

Article

Numerical Investigation into the Effects of a Viscous Fluid Seabed on Wave Scattering with a Fixed Rectangular Obstacle

Kuan-Yu Zheng, Chen-Wei Chang and I-Chi Chan *

Department of Civil Engineering, National Taiwan University, Taipei 10617, Taiwan

* Correspondence: ichichan@ntu.edu.tw

Abstract: We study numerically the effects of a viscous fluid seabed on wave scattering with a solid obstacle of rectangular shape fixed at the free surface, on the seafloor, or internally within the water layer. The computational model is based on OpenFOAM and it is validated using existing analytical solutions for waves encountering an obstacle on a solid bed and available experimental data for waves propagating over a muddy seabed with no obstacles. With the consideration of a solid obstacle on a viscous fluid bottom, we examine the corresponding transformations of incident, reflected, and transmitted wave components. The velocity field near the obstacle and the wave forces exerted on the obstacle are also analyzed. Our simulations show that all wave components experience significant amplitude attenuation caused by the viscous fluid bed. For both surface and bottom obstacles, the presence of an obstacle enhances the damping of reflected waves. When an internally submerged obstacle is considered, transmitted waves are the most affected due to a prominent vortex generated in the lee of the obstacle. Patterns of the velocity field in the vicinity of the obstacle are shown to be controlled mainly by the obstacle with some modulations in magnitude and wavelength contributed by the viscous fluid bed. In view of the vertical wave force on the obstacle surface, both a phase shift and decrease in magnitude are observed. These findings enhance our understanding of the underlying physical processes in the wave–obstacle–mud problems. More studies are still needed in order to provide the necessary technical tools for the engineering design of coastal structures in muddy marine environments.

Keywords: wave scattering; solid obstacle; viscous fluid seabed; OpenFOAM**MSC:** 76B15

Citation: Zheng, K.-Y.; Chang, C.-W.; Chan, I.-C. Numerical Investigation into the Effects of a Viscous Fluid Seabed on Wave Scattering with a Fixed Rectangular Obstacle.

Mathematics **2022**, *10*, 3911. <https://doi.org/10.3390/math10203911>

Academic Editors: Efstratios Tzirtzilakis and Yuri Shestopalov

Received: 1 September 2022

Accepted: 19 October 2022

Published: 21 October 2022

Publisher's Note: MDPI stays neutral with regard to jurisdictional claims in published maps and institutional affiliations.



Copyright: © 2022 by the authors. Licensee MDPI, Basel, Switzerland. This article is an open access article distributed under the terms and conditions of the Creative Commons Attribution (CC BY) license (<https://creativecommons.org/licenses/by/4.0/>).

1. Introduction

The hydrodynamic impact of coastal structures on the transmission of surface waves has always been a key subject in the study of water waves. The obstacles of interest often represent the common protective breakwaters, which are traditionally constructed as wave attenuators to defend our coasts from wave attacks and facilitate the navigation safety and operations in ports and harbors [1]. In wave–obstacle problems, the engineered structures can also appear in various forms as offshore oil drilling platforms [2], floating foundations of offshore wind turbines [3], underwater tube bridges for road traffic [4], heaving point absorbers for wave energy harvesting [5], or very large floating structures (VLFS), which have been regarded as a more sustainable engineering solution for coastal and offshore development than the traditional land reclamation approach [6].

In order to provide a scientific understanding of the effectiveness of these coastal structures and the potential impacts they may cause to the environment, many fundamental studies based on simplified obstacle geometry and idealized wave and seafloor conditions have been reported in the literature. For instance, within the framework of typical inviscid and irrotational assumptions for water waves, the scattering of linear progressive waves due to a rectangular obstacle either fixed at the free surface or resting on a flat solid seabed

was studied analytically by the method of eigenfunction expansions with both reflection and transmission coefficients, representing the most prominent scattering properties for practical engineering considerations, being obtained as functions of water depths, incident wave periods, and the physical dimensions of the obstacles [7]. Submerged obstacles of rectangular shape, i.e., a stationary structure situated internally within the water body, have also been studied analytically using the same mathematical technique of eigenfunction expansions [8–12], with the theoretical results revealing that, under a linear progressive wave, both reflection and transmission coefficients and the magnitude of wave forces exerted on the obstacle show oscillatory patterns with respect to the change in the obstacle length [11].

To further elucidate the hydrodynamics of wave–obstacle problems, more direct and telling observations were also made available by means of physical modeling, including wave flume experiments of regular and irregular waves encountering a surface obstacle [13–16], tests of propagation of linear progressive waves [17–20], solitary waves [21], and cnoidal waves [22] over a bottom standing obstacle, and laboratory studies of internally submerged obstacles under various types of incident waves [9,23–28]. These past experiments reported valuable wave gauge records of free surface elevation and measurements of wave force and dynamic pressure acting on the structures, which have been frequently used to examine the theoretically predicted reflection and transmission coefficients and wave forces exerted on the obstacles [7,9,10,20,29–31]. Furthermore, velocity measurements were also collected by nonintrusive techniques such as laser doppler velocimetry (LDV) [20] and particle image velocimetry (PIV) [21,22], providing direct evidence of vortex generation and shedding due to the obstacles that cannot be explained by the existing analytical models based on the potential flow assumption.

In addition to the analytical solutions and the laboratory experiments, many computational tools have also been developed for wave–obstacle problems to increase the modeling capability suitable for more complex and realistic conditions. Some notable numerical studies include the implementation of the Laplace equation for potential flow by the method of boundary integral equations [21,32] and finite element approximations [11,33], depth-integrated Boussinesq-type solvers for non-breaking [34,35] and breaking [36] long water waves, a two-dimensional Navier–Stokes solver by the finite-analytic method for nonbreaking waves [37], and a finite-difference-based model capable of simulating two-dimensional breaking waves by solving Reynolds-averaged Navier–Stokes (RANS) equations with additional parametrized models for turbulence closures and the volume of fluid method for capturing the free surface [38]. A more sophisticated RANS-based finite volume solver is also available for modeling three-dimensional wave–obstacle problems [39,40]. As far as the modeling of free-surface profiles is concerned, the existing numerical results have been shown to agree with laboratory data and analytical predictions [11,21,36,39].

Most existing theoretical studies of wave–obstacle problems are conventionally based on the assumption of a rigid and impermeable seabed. However, due to the complex and diverse compositions of marine sediments, natural seafloors can vary dramatically from solid rocky beds, to porous sandy bottoms characterized by noncohesive grains, to fluidized muddy seabeds comprised of cohesive sediments [41,42]. In fact, actual seafloors often respond to the significant dynamic pressures induced by surface waves, which may cause liquefaction and shear failure leading to the damage and even destruction of coastal structures [43]. To account for more realistic bottom conditions, seafloor flexibility and permeability have been considered by recent studies of surface waves responding to coastal structures on impermeable elastic beds [44–47], rigid porous bottoms [48–53], or poro-elastic seabeds [54–65]. In these studies, elastic seabeds are often modeled by the Euler–Bernoulli beam equation [44], rigid porous bottoms follow Darcy’s law [50], and poro-elastic effects are governed by Biot’s consolidation theory [54]. Due to the presence of an elastic bed, an interfacial wave with a shorter wavelength than the surface wave is generated by the surface wave loading and propagates along the water–seabed interface [44]. Reflection and transmission coefficients and the waveload on the structure are also affected by the

seabed conditions [46]. With the consideration of permeability and the inclusion of inertial resistances in the parameters representing porous effects, noticeable wave attenuation due to percolation is observed and the wave-induced pore pressure becomes weaker with the increase in seabed thickness [51,62]. In addition, excessive wave-induced upward seepage force inside the seabed leads to possible liquefaction, which may cause foundation failures of the coastal structures [43].

The above discussion suggests that wave scattering by coastal structures on solid, elastic, or sandy bottoms has been studied extensively. However, the literature on waves encountering obstacles above a muddy seabed composed of cohesive sediments is relatively scarce. In fact, muddy seafloors have been observed in many marine environments where the obstacles of interest may appear for various engineering purposes [42]. Field samples have also revealed that the flow and deformation characteristics of muddy deposits are fundamentally different from those of noncohesive sediment particles [42,66,67]. Hence, we believe that it is necessary to carefully examine the effects of a muddy seabed on wave scattering by an obstacle. In the present study, the wave–obstacle–mud problem is studied numerically. There exists a vast literature on the propagation and transformation of surface waves above a muddy bottom without encountering any coastal structures, where the rheological behaviors of bottom fluid mud have been idealized as Newtonian [66,68], viscoelastic [69,70], and viscoplastic [71,72] fluids. Conventionally, existing theoretical studies of wave–seabed interactions employed a two-layer system consisting of an upper inviscid water layer above a bottom muddy seabed laying on a solid ground [66,68–70]. It has been reported that interactions between surface waves and muddy seafloors lead not only to modifications of important wave characteristics such as wave celerity, wavelength, and wave height, but also significant motions of bottom cohesive sediments [66,70,71]. Evidently, this calls for the need to study wave–obstacle–mud interactions. Due partially to the diverse rheological properties of cohesive sediments, it is unrealistic to hope that the full spectrum of rheological behaviors of fluid mud can be described by a simple rheological model [42]. Therefore, in the present study we shall focus only on the scenarios where the bottom cohesive mud can be modeled as a Newtonian fluid. Adopting the canonical two-layer water–mud system, we perform a series of numerical simulations to investigate the effects of a viscous fluid bottom on wave scattering by a fixed obstacle placed at the free surface, on the seabed, or internally in the water layer. Key features, such as the reflection and transmission coefficients, velocity field in the vicinity of the obstacle, and the wave forces exerted on the obstacle, are presented and discussed.

The rest of the paper is organized as follows: In Section 2, we introduce the development and the validation of the numerical model used in the present study. Numerical results, including reflected and transmitted waves, velocity field, wave forces exerted on the obstacle, are presented and discussed in Section 3. Lastly, Section 4 summarizes the key findings of this study and discusses the limitations and possible improvements of the present numerical work.

2. Model Development

We introduce the computational model that is used to simulate the wave–obstacle–seabed problem, followed by the model validation using relevant analytical solutions and laboratory data available in the literature.

2.1. Assumptions and Simplifications

In the present wave–obstacle–mud problem, we adopted the two-layer system commonly used in the studies of wave–mud interactions [66], as shown in Figure 1. The upper layer is typical sea water and the bottom muddy seabed, which lays on an impermeable solid bed, is idealized by a Newtonian fluid. A fixed solid obstacle in the shape of a rectangle was considered. Three different settings were examined: a surface obstacle that is sufficiently high so that no wave overtopping is possible (Figure 1a); a bottom obstacle

sitting on the solid bed and penetrating through the water–mud interface (Figure 1b); a submerged obstacle resting internally in the water layer (Figure 1c).

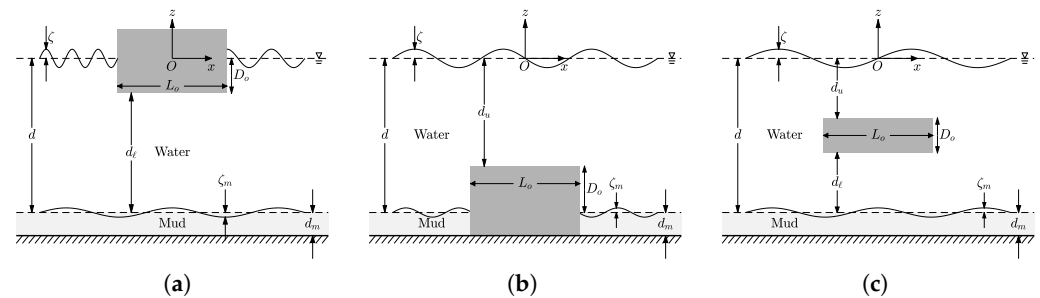


Figure 1. Schematic of wave scattering by a fixed obstacle above a fluid mud bottom: (a) surface obstacle; (b) bottom obstacle; (c) submerged obstacle. d = constant water depth before and after the obstacle. d_m = thickness of the mud layer. L_o, D_o = length and submerged depth of the obstacle. d_u, d_l = depths above and below the obstacle. ζ, ζ_m = displacements at the free-surface and the water–mud interface. (x, z) = horizontal and vertical coordinates.

2.2. Numerical Model

We constructed a numerical wave flume to investigate the scattering of periodic waves by a fixed rectangular obstacle above a fluid mud bottom. The computational model employs an open-source CFD suite *olaFlow* [73], which provides specialized functionality, such as boundary conditions for wave generation and active wave absorption, developed for water waves problems within the framework of the popular generic C++-based CFD software package *OpenFOAM* [74]. In the present study, we considered only laminar flows in two dimensions. Hence, *OpenFOAM* essentially solved the familiar 2D Navier–Stokes equations using an Eulerian finite volume discretization, where the fluid dynamic quantities were computed at the control volume centroids. Although, our simulations were limited to idealized 2D behaviors with waves normally incident on a rectangular obstacle over a simplified bathymetry, nonlinear interactions among waves, obstacles, and bottom fluid mud can be modeled as vertical variations of both velocity and pressure are taken into account by the 2D Navier–Stokes equations [40]. Since we needed to resolve motions of both water and bottom fluid mud, we utilized the solver *multiphaseInterFoam*, suitable for problems involving multiple incompressible fluids in the release *OpenFOAM* v2012, which is freely available at <https://www.openfoam.com> (last accessed on 8 August 2022). The PIMPLE algorithm, combining the pressure–velocity calculation procedure PISO (Pressure Implicit with Splitting of Operator) with the widely used iterative solution strategy SIMPLE (Semi-Implicit Method for Pressure-Linked Equations), was adopted in *OpenFOAM* to solve the finite volume discretized Navier–Stokes equations. In addition, fluid–fluid interfaces were modeled using the volume of fluid (VOF) method, a phase-fraction-based interface capturing technique that solves a species transport equation for the relative volume fraction of each fluid. In VOF, an interface is constructed by an isosurface of the volume fraction data with an isovalue that can be freely chosen between 0 and 1. In our simulations, both air–water and water–mud interfaces were defined by the isosurfaces at a value of 0.5.

The general layout of the 2D numerical wave flume considered in the present study is shown in Figure 2. The configuration includes inlet, propagation zone for incident and reflected waves, obstacle region, transmission zone, and finally a wave-absorbing boundary in the end of the domain. On all solid boundaries, the no-slip condition is imposed. As for the *inlet* condition, *waveType* regular and *waveTheory* Stokes I are set in *olaFlow* to generate a positive-going incident periodic wave. The utility *extendedRangeAWA* [75], which provides active wave absorption based on Airy wave theory for waves in water of arbitrary uniform depth, was implemented as the *outlet* condition to reduce spurious waves reflected at the end of the numerical wave tank. With the presence of a fluid mud bottom, *extendedRangeAWA* is not as effective as its original design for the case of a solid bottom.

To further minimize the interference due to reflections resulting from the wave-absorbing boundary, the obstacle region is sandwiched by two $3L$ long observation windows, where L is the wavelength of the incident wave, and the lengths of the propagation zone for incident and reflected waves and the transmission zone are both set at $9L$, as shown in Figure 2. Under this arrangement, we ensure that, for the purpose of wave scattering analysis, in our simulations at least 18 waves clean from the contamination of reflection can be recorded before and after the obstacle. Since we considered rectangular obstacles fixed in a typical wave flume, structured and uniform numerical mesh was generated directly by the use of the utility *blockmesh*. The required mesh resolution was determined through the validation with existing results, i.e., the examination on both wave scattering by an obstacle above a solid bed [7,11] and wave propagation over a viscous fluid bed without any obstacles [70]. The details of this process are discussed shortly in Section 2.3. In the present numerical study, a workstation equipped with two Intel Xeon E5-2620 v4 processors and 256 GB RAM was used. For a 4 m-long incident wave in water at a depth 0.8 m, a simulation of a 1 min event requires about 150 h wall clock time.

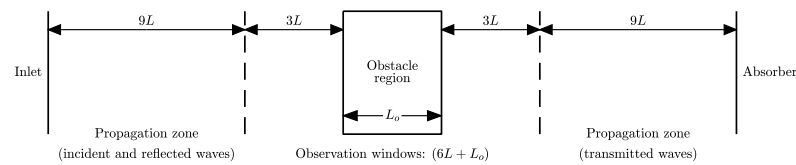


Figure 2. Layout of the present 2D numerical wave flume. L_o = length of the obstacle (see Figure 1). L = wavelength of the incident wave.

2.3. Model Validation

To examine the numerical implementation of the present model, we performed four tests relevant to the problem of interest. The first three cases consider waves above a solid bed, where scattering is due to a fixed free-surface [7], bottom [7], or submerged [11] obstacle. The final test regards waves over a soft seabed in the absence of obstacles [68,70,76]. In other words, these examples correspond to the problem sketched in Figure 1 but with either $d_m = 0$ (no mud) or $L_o = D_o = 0$ (no obstacle).

2.3.1. Surface Obstacle above a Solid Bed

We first consider the case of wave scattering due to a surface obstacle by examining the reflection and transmission coefficients, which are defined as the ratios of reflected wave amplitude and transmitted wave amplitude to the incident wave amplitude, respectively [7]. In order to determine the reflection coefficient from our numerical results, in the region before the obstacle it is necessary to decompose the incident waves and the reflected components from the simulated combined waves. Some techniques commonly used for the reflection analysis in physical wave flume testing include the two-point method employing fast Fourier transform to analyze records of wave spectra taken simultaneously at two adjacent stationary wave gauges [77], the N-gauge approach applying three or more stationary wave gauges with least squares optimization to minimize the noise signal for improved accuracy [78,79], and the use of Doppler analysis on free-surface data recorded by one or more continuously moving wave gauges [80]. We note that these methods are based on the assumption that the principle of superposition is applicable. In the present analysis, we adopted a more direct but time-consuming approach by performing additional trivial companion simulations for wave propagation without any obstacles. Hence, under the linear superposition, the reflection due to the obstacle can be readily deduced as

$$\eta_r = \eta - \eta_f, \tag{1}$$

where η is the simulated free-surface elevation for the wave-obstacle problem and η_f is the trivial free propagation wave also obtained numerically. Both η and η_f are model results under the identical numerical setups, except the later has no obstacles. Recall in

each simulation wave data over a length of 18 wave periods are recorded within a $3L$ -long observation window both before and after the obstacle, as indicated by the setup of the numerical wave tank illustrated in Figure 2. Therefore, when presenting the reflection and transmission coefficients, we further took a time average of the simulated wave data over the last eight wave periods since it requires a few waves for the simulations to become periodic.

Figure 3 shows the reflection and transmission coefficients obtained from both our simulations and the existing analytical solutions by the method of matched eigenfunction expansions [7]. The configuration of this surface obstacle example, as indicated in Figure 1a, has a water depth of $d = 0.8$ m, an obstacle of $L_o = D_o = 0.4$ m in dimensions, and $d_m = 0$ since a solid bed is considered. In our calculations, incident waves of various wave periods were examined. As can be expected, Figure 3 indicates that wave reflection becomes stronger for shorter waves, i.e., larger $k_0 D_o$ values with k_0 being the wavenumber of incident waves. Regarding the comparison between the present numerical results and the analytical predictions, the overall agreement is reasonable as the discrepancy becomes more noticeable but still acceptable for waves in shallower waters. In our simulations, we adopted a uniform mesh with $\Delta x = L/40$ in the horizontal direction and a vertical resolution of $\Delta z = 1/30$ m. The time step was determined accordingly by the Courant–Friedrichs–Lewy condition with the Courant number fixed at $C = 0.25$. We note that this C value is adopted throughout the present study.

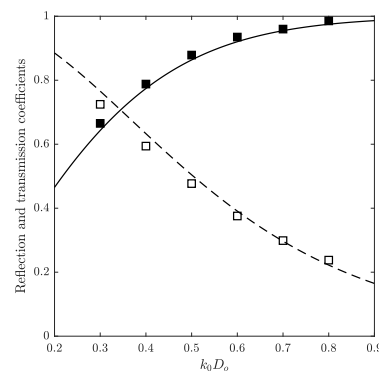


Figure 3. Wave scattering by a surface obstacle above a solid bed: reflection (■; solid line) and transmission (□; dashed line) coefficients. Symbols: present numerical results. Lines: analytical predictions reported in the literature [7]. k_0 represents the wavenumber of incident waves. $(d, D_o, L_o, d_m) = (0.8, 0.4, 0.4, 0)$ m are used in this example. See Figure 1a for the problem sketch.

2.3.2. Bottom Obstacle on a Solid Bed

We now examine the scattering of surface waves by a bottom obstacle illustrated in Figure 1b with $d_m = 0$. Both the reflection and transmission coefficients corresponding to $(d, D_o, L_o, d_m) = (0.8, 0.4, 0.4, 0)$ m are presented in Figure 4. We reiterate that the calculation of these two dimensionless coefficients is described in Section 2.3.1. The oscillatory nature of the reflection coefficient shown in Figure 4, which is very different from the monotonic behavior for the case of a surface obstacle presented in Figure 3, is due to the interference between the two ends of the obstacle [7]. Figure 4 also suggests that our numerical results are in satisfactory agreement with the available analytical calculations obtained again by the eigenfunction expansions [7]. In this example, the temporal and spatial resolutions are the same as those used in Figure 3 for a surface obstacle.

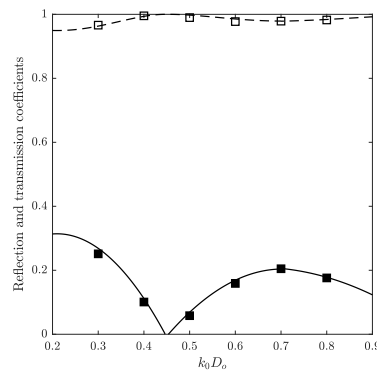


Figure 4. Bottom obstacle on a solid bed: reflection (■; solid line) and transmission (□; dashed line) coefficients. Symbols: numerical results. Lines: existing analytical predictions [7]. k_0 is the wavenumber of incident waves. In this example, $(d, D_o, L_o, d_m) = (0.8, 0.4, 0.4, 0)$ m. See Figure 1b for the problem sketch.

2.3.3. Submerged Obstacle above a Solid Bottom

Figure 5 plots the results for the case of a submerged obstacle sketched in Figure 1c with $d_m = 0$. In this example, $(d, D_o, d_\ell) = (0.8, 0.02, 0.54)$ m and the incident wave period is fixed at $T = 1.79$ s. In panel (a) of the figure, we present both the reflection and transmission coefficients, while panel (b) shows the dimensionless horizontal and vertical forces exerted on the obstacle. The dimensionless wave force components are defined as [11]

$$\bar{F}_x = \max\left(\frac{|F_x|}{\rho g a_0 D_o}\right) \tag{2}$$

and

$$\bar{F}_y = \max\left(\frac{|F_y|}{\rho g a_0 L_o}\right), \tag{3}$$

where ρ is the density of water, g is the gravitational acceleration, a_0 is the amplitude of incident waves, and the horizontal and vertical wave forces erected on the obstacle, F_x and F_y , are calculated by integrating the pressure, p , obtained by our simulations over the surface area of the obstacle, Γ_o , as [11]

$$F_x = \int_{\Gamma_o} p n_x ds \tag{4}$$

and

$$F_y = \int_{\Gamma_o} p n_y ds, \tag{5}$$

respectively, where $\vec{n} = (n_x, n_y)$ is the normal direction of the obstacle boundary. In our 2D simulations, F_x and F_y are wave forces per unit width of the wave flume. We note that F_x and F_y are functions of time, whereas the dimensionless coefficients \bar{F}_x and \bar{F}_y , which represent the maximum quantities, are time-independent.

As shown in Figure 5, the oscillatory feature is evident for both the reflection coefficient and dimensionless horizontal wave force acting on the obstacle, which is similar to the case of a bottom obstacle presented in Figure 4. Figure 5 also compares our simulations with the existing analytical predictions [11], suggesting that the two results are comparable. We note that, in this example, we adopted $\Delta x = L/80$ and $\Delta z = 0.01$ m for the numerical mesh.

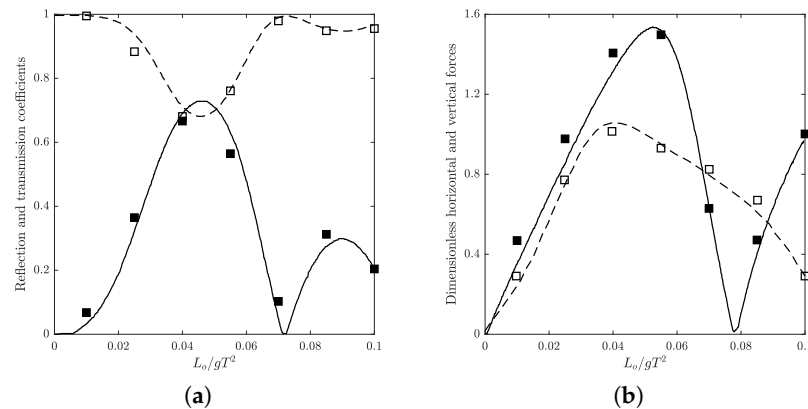


Figure 5. Wave scattering by a submerged obstacle above a solid bed: (a) reflection (■; solid line) and transmission (□; dashed line) coefficients; (b) dimensionless horizontal (■; solid line) and vertical (□; dashed line) forces acting on the obstacle, as defined in (2) and (3), respectively. Symbols: numerical simulations. Lines: analytical results reported in the literature [11]. In this case, $(d, D_o, d_\ell, d_m) = (0.8, 0.02, 0.54, 0)$ m and the incident wave period is $T = 1.79$ s. See Figure 1c for the problem sketch.

2.3.4. Waves over a Layer of Viscous Fluid Mud

The case of periodic waves propagating over a viscous fluid bottom without any obstacles, i.e., setting $L_o = D_o = 0$ in Figure 1, is now considered. Our model predictions are compared with the existing analytical results [68,70] and laboratory data [76] reported in the literature. In Figure 6, we plot the amplitude ratio, a/a_0 , as a function of dimensionless propagation distance, x/L , to demonstrate the effects of a viscous fluid bed on wave propagation. In this example, an incident wave of $T = 1.79$ s in a constant depth of $d = 0.8$ m is considered. The fluid mud has a viscosity of $\nu_m = 0.003$ m²/s and density $\rho_m = 1111$ kg/m³. In addition, the thickness of the muddy bed, d_m , is equal to the Stokes boundary layer thickness of mud, i.e., $d_m = \delta_m = 0.0413$ m. As shown in Figure 6, we observe a 20% attenuation in wave amplitude over a propagation distance of six wavelengths, suggesting a strong wave damping due to the presence of a fluid bottom. Amplitude attenuation is in fact the most dominant effect caused a viscous muddy bed [68,70]. We reiterate that our numerical results are time-averaged over the last 8 wave periods as discussed previously in Section 2.3.1. For comparison, in Figure 6 we also plot the analytical predictions of wave attenuation obtained by using a two-layer Stokes’ boundary layer model [70]. As can be seen, two results agree favorably with each other. In our numerical simulations, $\Delta x = L/200$ and $\Delta z = 0.0025$ m are used.

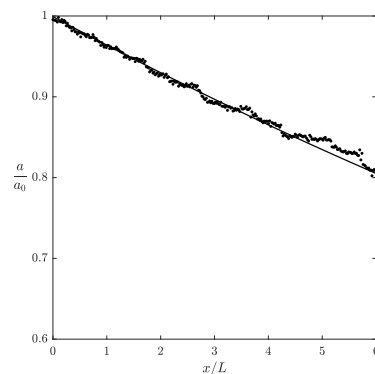


Figure 6. Waves over a viscous fluid bottom without obstacles: amplitude ratio, a/a_0 , as a function of dimensionless propagation distance, x/L . Dot: present numerical results. Line: existing analytical predictions [70]. In this example, $T = 1.79$ s, $d = 0.8$ m, $\nu_m = 0.003$ m²/s, $\rho_m = 1111$ kg/m³, and $d_m = 0.0413$ m.

In Figure 7, we compare simulated horizontal velocities at five different elevations with experimental data available in the literature [76]. In the laboratory testing, the viscous fluid mud bed was $d_m = 0.11$ m thick. At a fixed horizontal location 1 m away from the beginning edge of the model mud bed used in the experiment, five electromagnetic flowmeters were placed vertically across the mud layer and the water body to record flow velocity. Among these flowmeters, three were installed at 0.025, 0.06, and 0.09 m below the undisturbed water–mud interface while the remaining two were fixed at 0.01 and 0.04 m above the interface [76]. Other key experimental conditions were: $T = 1.3$ s, $a_0 = 0.025$ m, $d = 0.3$ m, $\nu_m = 0.03$ m²/s, and $\rho_m = 1294.7$ kg/m³ [76]. In addition to the present numerical results and the laboratory measurements [76], Figure 7 also plots the existing analytical predictions [68] for comparison. As can be seen in the figure, mud flow velocity (bottom three panels in Figure 7) is much weaker than the water particle velocity (top two panels) and two velocities are slightly out of phase. In general, our simulations agree fairly with the measurements although difference is evident at 0.09 m below the interface. It is interesting to see that our results agree almost perfectly with the analytical solutions obtained by solving the linearized Navier–Stokes equations in a two-layer viscous fluid system [68]. We note that in the numerical simulations the temporal and spatial resolutions are the same as those used in Figure 6.

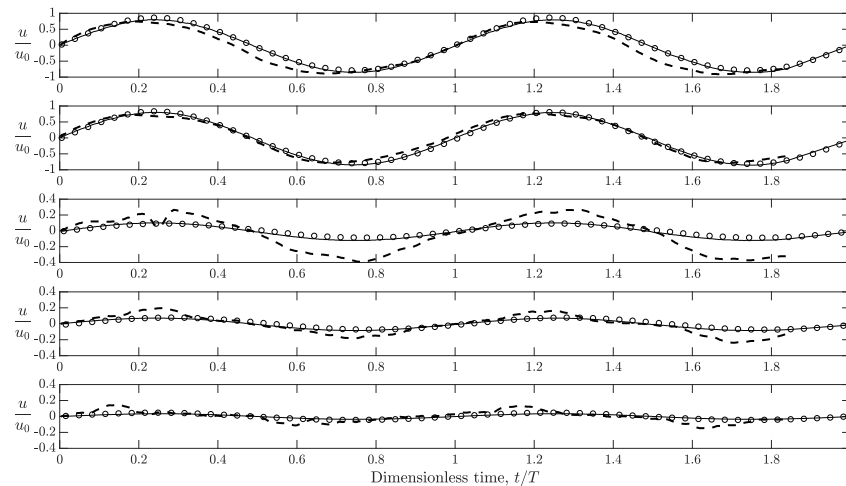


Figure 7. Time histories of horizontal velocity, u , at five different elevations. The velocity is normalized by the characteristic wave-induced velocity, $u_0 = a_0(2\pi/T)$. The first and the second panels show the results at 0.04 and 0.01 m above the initial water–mud interface, respectively. The remaining three panels, from top to bottom, plot the velocity at 0.025, 0.06, and 0.09 m below the interface. Circle: present numerical results. Dashed line: laboratory data [76]. Solid line: existing analytical solutions [68]. In this example, $T = 1.3$ s, $a_0 = 0.025$ m, $d = 0.3$ m, $d_m = 0.11$ m, $\nu_m = 0.03$ m²/s, $\rho_m = 1294.7$ kg/m³, and $u_0 = 0.12$ m/s. Records of experimental data were slightly less than two wave periods.

Through the above validation testing, we have demonstrated the capability of the present model to simulate both wave scattering by an obstacle on a solid bed and wave propagation above a viscous fluid bed without any obstacles. In the process, we have gained the experience on the numerical resolution requirements necessary for a satisfactory comparison, which is valuable for us to study the full problem of the impacts of a viscous fluid bottom on scattering of periodic waves by a fixed rectangular obstacle as illustrated in Figure 1.

3. Results and Discussions

We shall now present and discuss the numerical results for three exemplary cases of the wave–obstacle–mud problem. Specifically, variation of wave amplitudes, wave forces erected on the obstacle, and velocity fields surrounding the obstacle are analyzed to

evaluate the effects of a viscous fluid bed on wave scattering by a fixed surface, bottom, or submerged obstacle. We reiterate that the problem of interest is sketched in Figure 1 and the configuration of the 2D numerical wave flume can be read in Figure 2. Suggested by the validation tests discussed in Section 2.3, all the numerical results presented herein are obtained under the setup of $\Delta x = L/200$ and $\Delta z = 0.0025$ m. Furthermore, the decomposition and time averaging of incident waves and reflected components follow the procedures introduced in Section 2.3.1. For the calculations of wave forces, they have been defined in Section 2.3.3.

3.1. Surface Obstacle

We first discuss the case of a surface obstacle above a viscous fluid bottom, as defined in Figure 1a. Spatial variations of wave amplitude ratio, a/a_0 , within the observation windows before and after the obstacle are shown in Figure 8. In our simulations, we consider $T = 1.79$ s, $a_0 = 0.02$ m, $d = 0.8$ m, $\nu_m = 0.003$ m²/s, $\rho_m = 1111$ kg/m³, $L_o = 0.8$ m, and $D_o = 0.4$. To evaluate the effects of mud layer thickness, results for $d_m = 0$, δ_m , and $3\delta_m$ are plotted in the same figure for comparison. As can be seen from the results of these three cases presented in Figure 8, in the region before the obstacle the simulated wave amplitudes, which combine both incident and reflected components, oscillate between $a/a_0 = 0.1$ and 1.75, indicating the phase shift of incident waves and reflected waves. We also observe that, with the presence of a muddy bed, the combined waves tend to be flattened out due to the viscous damping within the mud layer, where the wave amplitudes become smaller and the wavelengths get longer. On the other hand, in the region after the obstacle the transmitted wave displays a pattern of continuous attenuation of wave amplitude, which is similar to the validating testing presented in Section 2.3.4 for waves over a layer of viscous fluid mud with no obstacles.

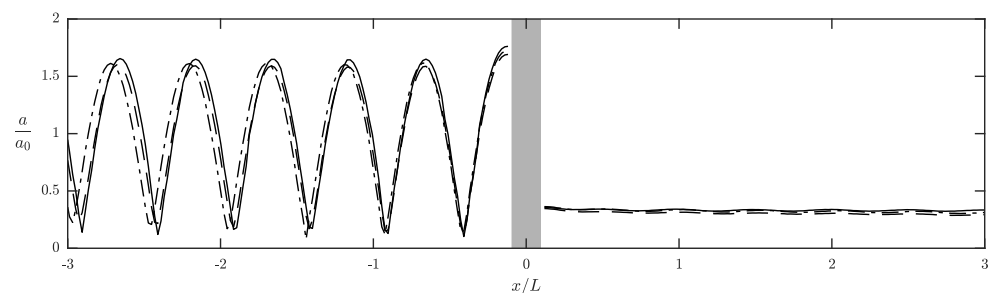


Figure 8. Effects of mud layer thickness on wave scattering by a surface obstacle: spatial variation of wave amplitude ratio, a/a_0 . Solid line: $d_m = 0$ (solid bottom). Dashed line: $d_m = \delta_m$. Dashed-dotted line: $d_m = 3\delta_m$. Shaded box denotes the surface obstacle. In this case, $T = 1.79$ s, $a_0 = 0.02$ m, $d = 0.8$ m, $\nu_m = 0.003$ m²/s, $\rho_m = 1111$ kg/m³, $L_o = 0.8$ m, and $D_o = 0.4$ m. See Figure 1a for the problem definition.

In Figure 9a, we show the decomposed incident waves and reflected waves corresponding to the results with different mud layer thicknesses presented in Figure 8. For the case of a solid bed ($d_m = 0$), the amplitudes decrease only slightly as waves propagate towards or away from the obstacle, with around 2% changes over two wavelengths as shown in the figure. When a viscous fluid bed ($d_m > 0$) is considered, by contrast, considerable wave amplitude attenuation is observed for both incident and reflected components. For $d_m = \delta_m$, the amplitude of incident wave decreases 7.5% over a propagation distance of $2L$ while the amplitude variation for reflected wave is 15.5%. For a thicker mud with $d = 3\delta_m$, the attenuation of wave amplitude becomes weaker, dropping to 5.8% and 7.9% for incident and reflected waves, respectively. In Figure 9b, we take a closer look at the corresponding transmitted waves in the region after the obstacle. We observe that for the cases with $d_m = 0$, δ_m , and $3\delta_m$ the changes of amplitudes over distance $2L$ are, respectively, 2.0%, 7.0% and 5.1%. We reiterate that for waves propagating over a fluid mud bed without any obstacles, the attenuation of wave amplitude over $2L$ is 7.2% as shown in Figure 6.

This implies that for the case of a surface obstacle the incident and transmitted waves experience the same wave damping as if there was no obstacle. The results illustrated in Figure 9 also indicate that, across all wave components, the largest damping rate occurs at $d_m = \delta_m$, which is in agreement with the existing laboratory study [66] and analytical modeling [68,70] all showing that an extreme wave attenuation rate is possible when the mud layer thickness is about the Stokes boundary layer thickness of mud.

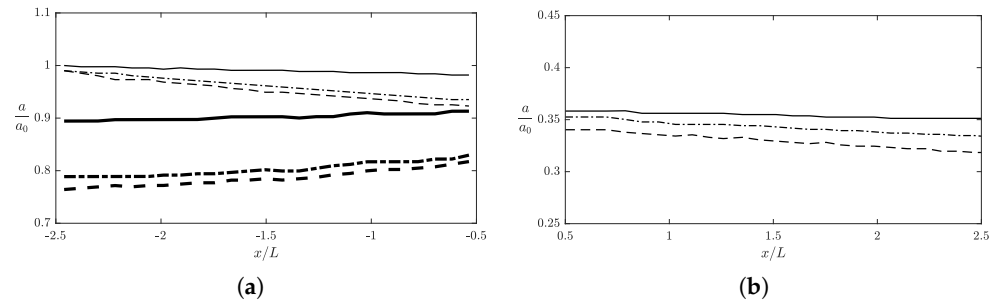


Figure 9. Wave components corresponding to the amplitude variation shown in Figure 8: (a) incident waves (thin lines) and reflected components (thick lines); (b) transmitted waves. Solid lines: $d_m = 0$ (solid bottom). Dashed lines: $d_m = \delta_m$. Dashed-dotted lines: $d_m = 3\delta_m$. See Figure 8 for the model inputs.

Figure 10 examines the velocity field surrounding the obstacle for $d_m = 0$. We present the snapshots at equally spaced time instants within a wave period, i.e., $t/T = \frac{1}{6}, \frac{2}{6}, \frac{3}{6}, \frac{4}{6},$ and $\frac{5}{6}$. Similar results for $d_m = 3\delta_m$ are plotted in Figure 11. The corresponding free-surface profiles are also indicated in the figures. Comparing these two sets of results, we observe that the flows exhibit similar pattern for both solid bed ($d_m = 0$) and muddy bed ($d_m = 3\delta_m$), suggesting that the main feature of the velocity distribution is controlled by the obstacle with modulations in magnitude and wavelength contributed by the presence of a muddy bed.

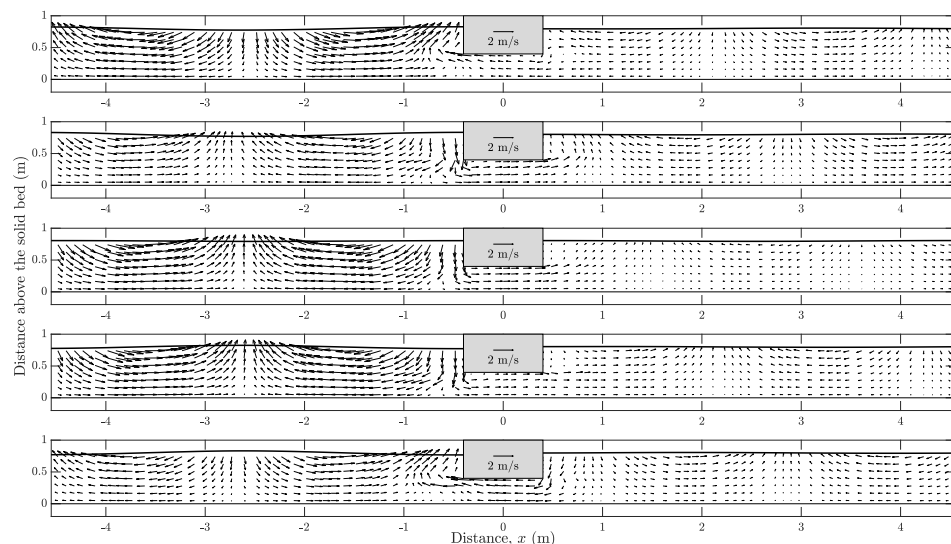


Figure 10. Surface obstacle on a solid bed ($d_m = 0$): snapshots of velocity field at six time instants over a wave period. Top to bottom: $t/T = \frac{1}{6}, \frac{2}{6}, \frac{3}{6}, \frac{4}{6},$ and $\frac{5}{6}$. Solid line indicates the free surface. The arrow inside the obstacle shows the reference magnitude. See Figure 8 for the model inputs.

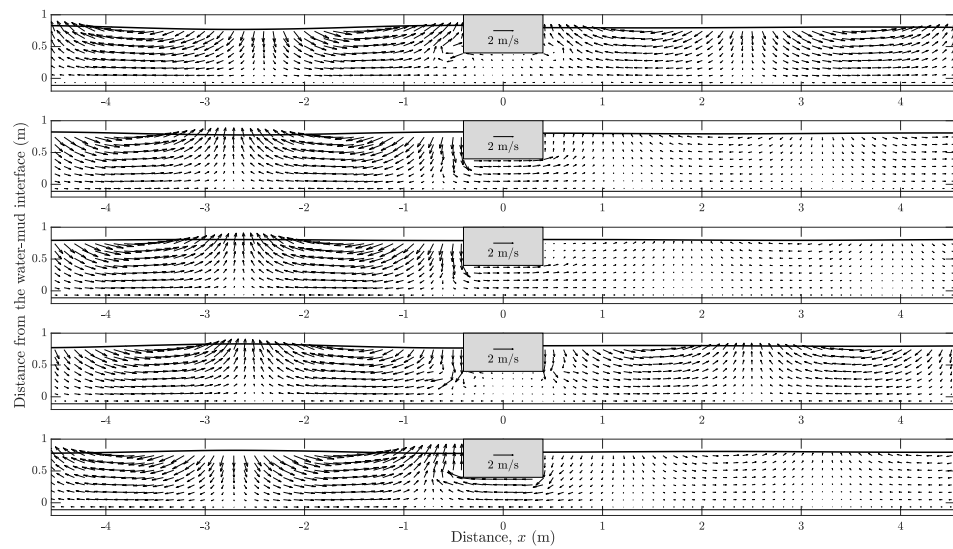


Figure 11. Snapshots of velocity field due to a surface obstacle on a muddy bed with $d_m = 3\delta_m$. Top to bottom: $t/T = \frac{1}{6}, \frac{2}{6}, \frac{3}{6}, \frac{4}{6},$ and $\frac{5}{6}$. Solid line indicates the free surface. See Figure 8 for the model inputs.

In Figure 12, we show the time histories of dimensionless vertical wave force exerted on the bottom of the surface obstacle with $d_m = 0, \delta_m,$ and $3\delta_m$. The dimensionless force component is obtained by first calculating the vertical wave force, F_y , using (5) and then normalizing the dimensional F_y by the characteristic wave force, $\rho g a_0 L_o$. Results presented in the figure suggest considerable phase shift caused by a muddy bed. In this example, we observe a larger phase difference for the case of a thicker mud layer, i.e., when $d_m = 3\delta_m$.

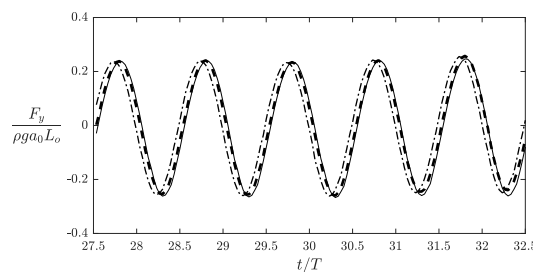


Figure 12. Time histories of dimensionless vertical force acting on the bottom of a surface obstacle. Solid line: $d_m = 0$ (solid bottom). Dashed line: $d_m = \delta_m$. Dashed-dotted line: $d_m = 3\delta_m$. The dimensional force F_y is given in (5). See Figure 8 for other model inputs.

3.2. Bottom Obstacle

We continue to examine the effects of a fluid bed on wave scattering by a bottom obstacle of dimensions $L_o = 1.6$ m and $D_o = 0.4$ m as illustrated in Figure 1b. In our simulations, we consider an incident wave of $T = 1.79$ s and $a_0 = 0.02$ m in a constant depth of $d = 0.8$ m. The viscous mud has the properties of $\nu_m = 0.003$ m²/s and $\rho_m = 1111$ kg/m³. Three different cases with $d_m = 0$ (solid bed), $\delta_m,$ and $3\delta_m$ are simulated. In Figure 13, we plot the spatial variation of dimensionless wave amplitudes, a/a_0 , corresponding to these three mud layer thicknesses. As can be seen, for the cases with $d_m > 0$ considerable amplitude attenuation is persistent after waves passing the obstacle. On the other hand, in the region before the bottom obstacle the oscillation in wave amplitude suggests the phase difference between the incident and reflected components. Figure 14a plots the decomposed incident waves and reflected waves corresponding to the combined waves presented in Figure 13. Our results show that, over a propagation distance of $2L$, the incident waves experience a 1.7%, 7.5%, and 5.7% decrease in wave amplitude for $d_m = 0, \delta_m,$ and $3\delta_m$. Regarding the reflected waves, the changes are higher at 4.0%, 14.5%, and 10.2%,

respectively. For the transmitted wave presented in Figure 14b, the amplitude attenuation over $2L$ is 1.7% for $d_m = 0$, 7.3% for $d_m = \delta_m$, and 6.4% for $d_m = 3\delta_m$. Similar to the case of a surface obstacle discussed in Section 3.1, these results again suggest that the bottom obstacle has little impact on the mud-induced damping of both incident and transmitted waves. However, the reflected waves experience much stronger wave attenuation. In addition, the largest damping rate occurs at $d_m = \delta_m$ for all wave components.

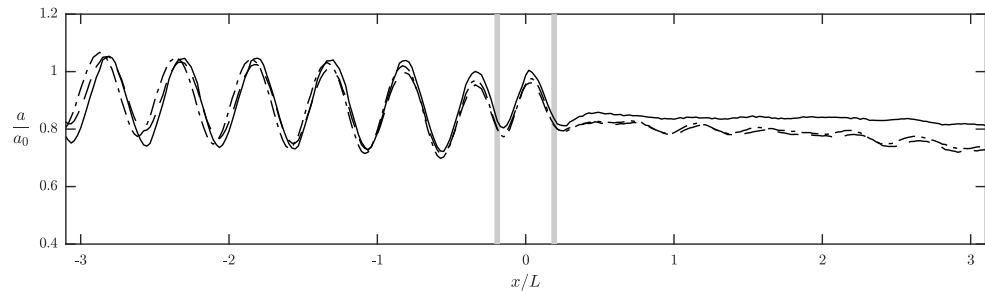


Figure 13. Spatial variation of amplitude ratio, a/a_0 , due to a bottom obstacle above a muddy bed with different thicknesses. Solid lines: $d_m = 0$ (solid bottom). Dashed lines: $d_m = \delta_m$. Dashed-dotted lines: $d_m = 3\delta_m$. Vertical bars indicate the location of the bottom obstacle. In this case, $T = 1.79$ s, $a_0 = 0.02$ m, $d = 0.8$ m, $\nu_m = 0.003$ m²/s, $\rho_m = 1111$ kg/m³, $L_o = 1.6$ m, and $D_o = 0.4$ m. See Figure 1b for the problem definition.

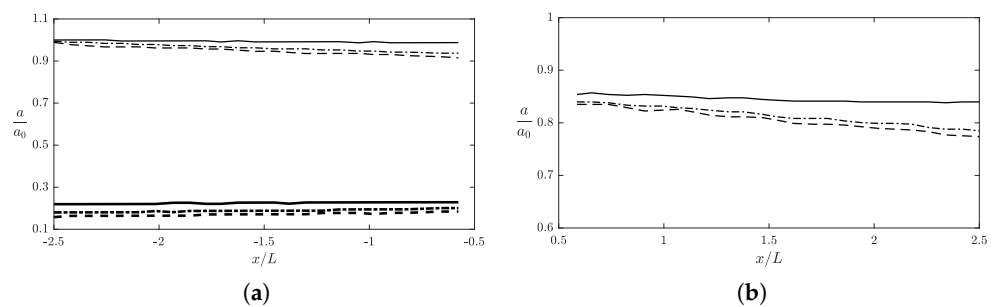


Figure 14. Wave components corresponding to the case of a bottom obstacle shown in Figure 13: (a) incident waves (thin lines) and reflected components (thick lines); (b) transmitted waves. Solid lines: $d_m = 0$ (solid bottom). Dashed lines: $d_m = \delta_m$. Dashed-dotted lines: $d_m = 3\delta_m$. Vertical bars indicate the location of the bottom obstacle. See Figure 13 for the model inputs.

In Figures 15 and 16, we plot the velocity field in the neighborhood of the obstacle for $d_m = 0$ and $d_m = 3\delta_m$, respectively. Comparing the snapshots of velocity in these two figures, we observe that, although the flow patterns look similar, due to the presence of a fluid bottom the phase shift and the increase in wavelength are both evident. This again shows the roles of the obstacle and the mud bed in shaping the velocity distribution.

Figure 17 shows the time histories of dimensionless vertical wave force acting on the top of the bottom obstacle under three different scenarios with $d_m = 0$, δ_m , and $3\delta_m$, respectively. Phase lag due to the presence of the mud layer is again observed in the figure. Furthermore, the phase difference is more considerable when $d_m = 3\delta_m$.

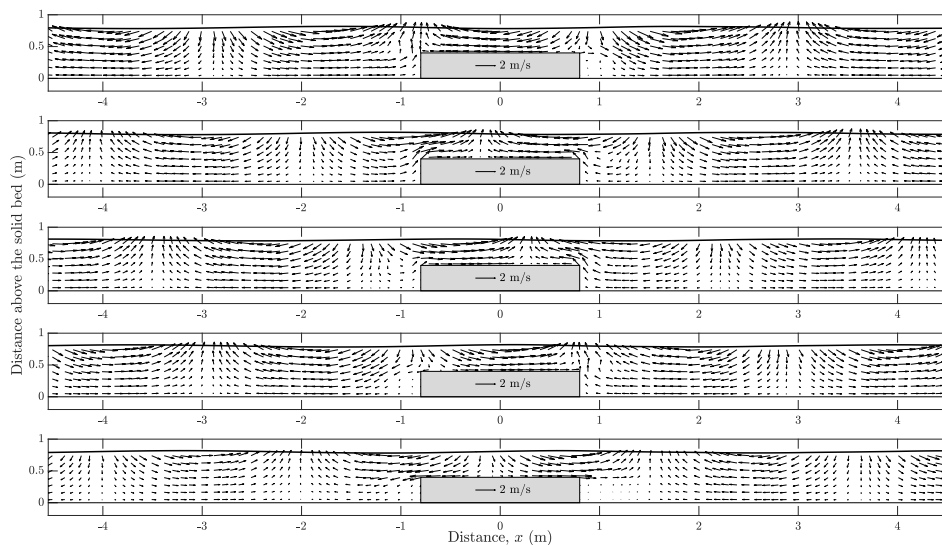


Figure 15. Snapshots of velocity field due to a bottom obstacle on a solid bed ($d_m = 0$) at six time instants over a wave period. Top to bottom: $t/T = \frac{1}{6}, \frac{2}{6}, \frac{3}{6}, \frac{4}{6},$ and $\frac{5}{6}$. Solid line indicates the free surface. See Figure 13 for the model inputs.

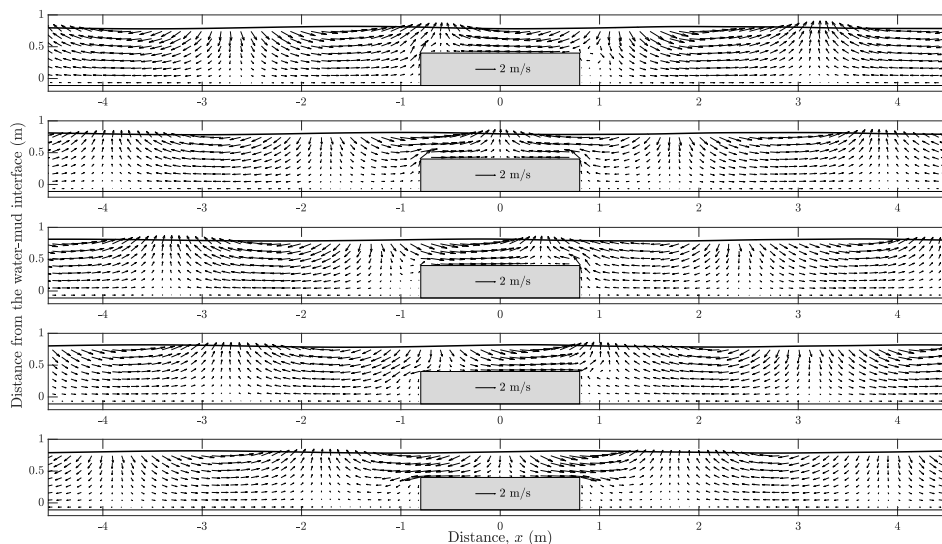


Figure 16. Bottom obstacle on a muddy bed with $d_m = 3\delta_m$: snapshots of velocity field over a wave period at $t/T = \frac{1}{6}, \frac{2}{6}, \frac{3}{6}, \frac{4}{6},$ and $\frac{5}{6}$ (top to bottom). Solid line indicates the free surface. See Figure 13 for the model inputs.

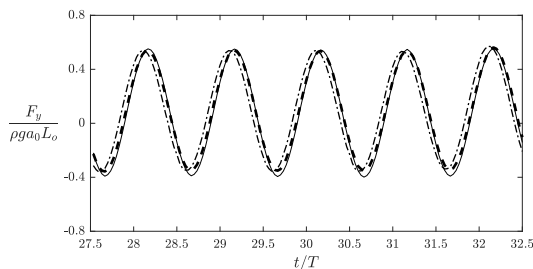


Figure 17. Time histories of dimensionless vertical force acting on the top of a bottom obstacle with $d_m = 0$ (solid line), $d_m = \delta_m$ (dashed line), and $d_m = 3\delta_m$ (dashed-dotted line). See Figure 13 for other model inputs.

3.3. Submerged Obstacle

Lastly, we discuss the case of a submerged obstacle as illustrated in Figure 1c with $(L_o, D_o, d_\ell) = (1.2529, 0.02, 0.54)$ m. For convenient, we consider again an incident wave of $T = 1.79$ s and $a_0 = 0.02$ m in water of depth $d = 0.8$ m. Regarding the properties of viscous fluid mud, $\nu_m = 0.003$ m²/s and $\rho_m = 1111$ kg/m³. In addition, three different cases with $d_m = 0, \delta_m,$ and $3\delta_m$ are examined to evaluate the effects of mud layer thickness. In Figure 18, we plot the spatial variation of dimensionless amplitude, a/a_0 , showing the amplitude attenuation and phase shift caused by the muddy bed and a sudden change in wave amplitude due to the obstacle. Figure 19a shows the decomposed incident and reflected components corresponding to the simulated combined waves presented in Figure 18. For the incident waves, we observe a 2.0%, 7.8%, and 6.4% decrease in wave amplitude over a propagation distance of two wavelengths corresponding to $d_m = 0, \delta_m,$ and $3\delta_m$. Similarly, the changes of wave amplitude for the reflected components are comparable at 2.3%, 8.7%, and 5.7%, respectively. Our results show again a strong damping caused by the bottom fluid med. Moreover, the largest damping rate occurs when $d_m = \delta_m$. Regarding the transmitted waves presented in Figure 19b, it is shown that the amplitude variation over $2L$ is significantly higher at 13.1% for $d_m = 0$, 18.3% for $d_m = \delta_m$, and 16.6% for $d_m = 3\delta_m$. This is very different from the observations of both surface and bottom obstacles presented in Figure 9b and Figure 14b, respectively. In this example, the unexpected large change in wave amplitude, especially over 10% for the case of a solid bottom ($d_m = 0$), is mainly attributed to the effects of vortex generation due to the shape edges of the obstacle [20,21]. This amplitude variation can not be explained solely as the wave damping by the viscous mud. The behavior can be better understood by examining the velocity field and is discussed in the following.

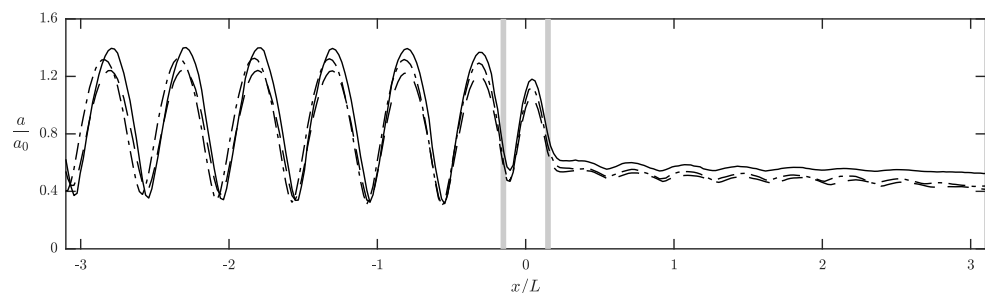


Figure 18. Effects of mud layer thickness on wave scattering by a submerged obstacle: spatial variation of amplitude ratio, a/a_0 . Solid lines: $d_m = 0$ (solid bottom). Dashed lines: $d_m = \delta_m$. Dashed-dotted lines: $d_m = 3\delta_m$. Vertical bars indicate the location of the obstacle. In this case, $T = 1.79$ s, $a_0 = 0.02$ m, $d = 0.8$ m, $d_u = 0.24$ m, $d_\ell = 0.54$ m, $\nu_m = 0.003$ m²/s, $\rho_m = 1111$ kg/m³, $L_o = 1.2529$ m, and $D_o = 0.02$ m. See Figure 1c for the problem definition.

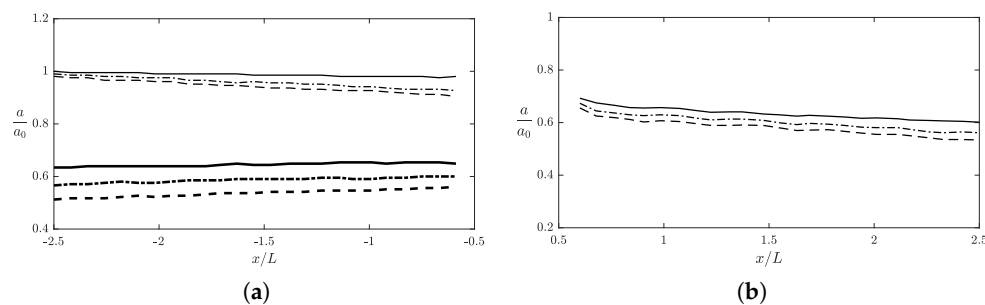


Figure 19. Wave components corresponding to the case of a submerged obstacle shown in Figure 18: (a) incident waves (thin lines) and reflected components (thick lines); (b) transmitted waves. Solid lines: $d_m = 0$ (solid bottom). Dashed lines: $d_m = \delta_m$. Dashed-dotted lines: $d_m = 3\delta_m$. Vertical bars indicate the location of the obstacle. See Figure 18 for the model inputs.

The associated velocity field for the case of a submerged obstacle above a solid bottom is plotted in Figure 20. The figure, which presents the snapshots at several equally spaced time instants within a wave period, reveals large velocity gradients in both horizontal and vertical directions around the leading edge of the obstacle. Furthermore, in the lee of the obstacle a prominent clockwise vortex is formed. The flow pattern shown in Figure 20 is similar to the laboratory observations of waves passing over a bottom obstacle on a solid bed [20,21]. In Figure 21, we present the velocity field with the consideration of a muddy bed with $d_m = 3\delta_m$. Comparing with the results shown in Figure 20 for the case of a solid bed, the size of the vortex core is considerably smaller when the effects of viscous fluid mud bed are taken into account. In addition, an obvious phase difference on the formation of the vortex is observed.

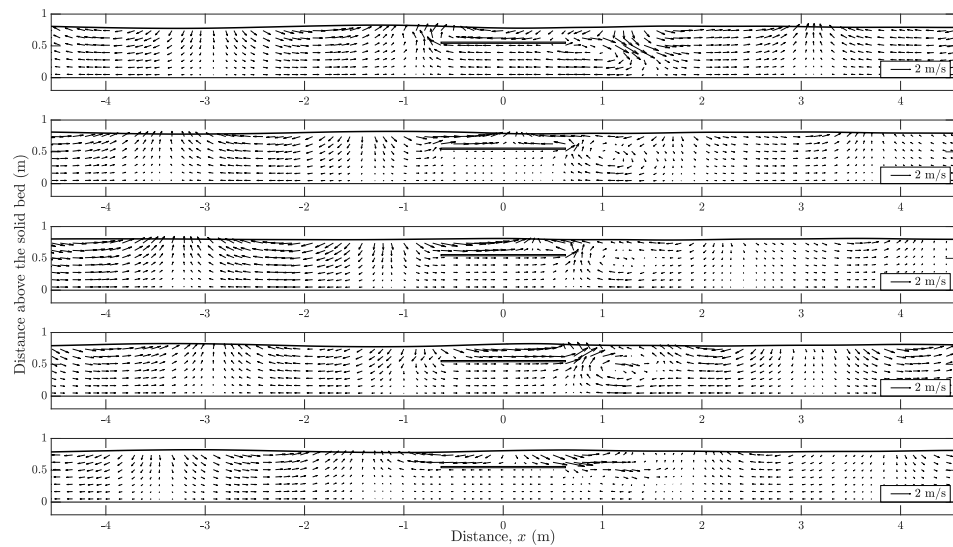


Figure 20. Submerged obstacle on a solid bed ($d_m = 0$): snapshots of velocity field over a wave period at $t/T = \frac{1}{6}, \frac{2}{6}, \frac{3}{6}, \frac{4}{6},$ and $\frac{5}{6}$ (top to bottom). Solid line indicates the free surface. See Figure 18 for the model inputs.

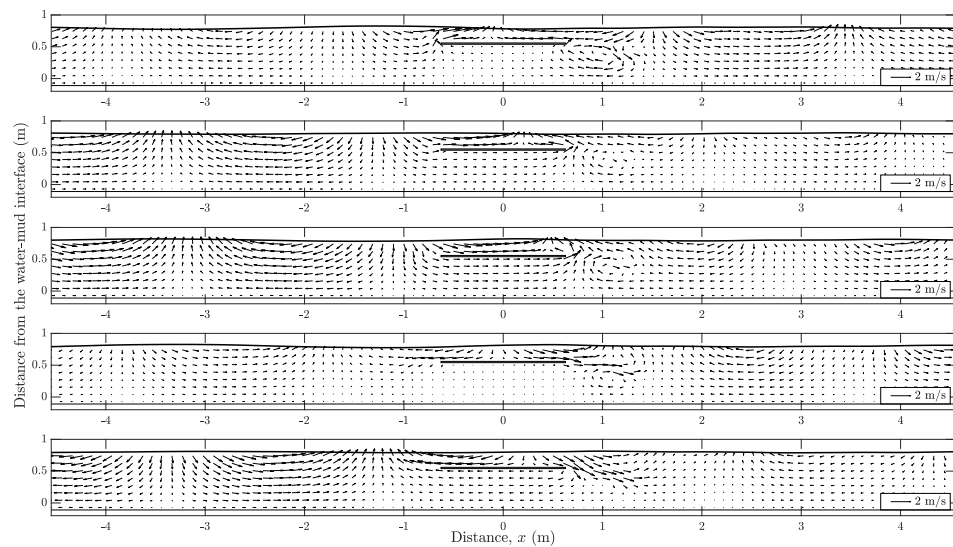


Figure 21. Snapshots of velocity field due to a submerged obstacle on a muddy bed with $d_m = 3\delta_m$. Top to bottom: $t/T = \frac{1}{6}, \frac{2}{6}, \frac{3}{6}, \frac{4}{6},$ and $\frac{5}{6}$. Solid line indicates the free surface. See Figure 18 for the model inputs.

In Figure 22, we examine the effects of a muddy bed by showing the time histories of dimensionless vertical wave acting on the submerged obstacle under different mud layer thickness, namely $d_m = 0, \delta_m,$ and $3\delta_m$. We recall the vertical force, F_y , is calculated by (5).

Results presented in Figure 22 reveal that, due to the presence of a muddy bed, the magnitude of vertical force becomes smaller and the phase difference is also considerable. In this example, the case with $d_m = \delta_m$ shows a larger decrease in wave force whereas the phase shift is more substantial for a thicker layer with $d_m = 3\delta_m$.

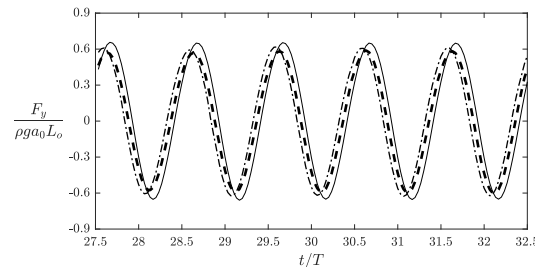


Figure 22. Time histories of dimensionless vertical force exerted on a submerged obstacle. Solid line: $d_m = 0$ (solid bottom). Dashed line: $d_m = \delta_m$. Dashed-dotted line: $d_m = 3\delta_m$. See Figure 18 for other model inputs.

4. Concluding Remarks

We present a numerical study to investigate the effects of a viscous fluid bed on wave scattering by a fixed surface, bottom, or submerged obstacle of rectangular shape. Numerical simulations are realized by an OpenFOAM-based computational model for wave–obstacle–seabed problem. Limited by our computation resources, we focused only on two-dimensional flows. Our numerical model was validated using existing analytical and experimental results for wave scattering by an obstacle on a solid bed and wave propagation over a muddy seabed without any obstacles. Under the influence of a muddy seabed, we examined the features of reflected and transmitted waves, velocity fields, and wave forces exerted on the obstacle. Based on our numerical results, the following main findings are reported:

1. Surface obstacle: Section 3.1

- Incident and transmitted wave components show an amplitude attenuation rate similar to the case of waves over a muddy bed without any obstacles. Reflected waves have a much stronger damping rate.
- For incident, reflected, and transmitted wave components, the largest damping rates all occur at $d_m = \delta_m$.
- The pattern of the velocity distribution is mainly controlled by the obstacle with modulation in magnitude and wavelength contributed by the muddy bed.
- In terms of the dimensionless vertical wave force exerted on the obstacle surface, a larger phase difference was observed for the case of a thicker mud layer.

2. Bottom obstacle: Section 3.2

- The effect of bottom obstacle on mud-induced amplitude attenuation is only considerable for the reflected wave components.
- The largest wave damping of each wave component was observed when the mud layer thickness was $d_m = \delta_m$.
- The impact of viscous fluid bed on the flow pattern in the vicinity of the obstacle was not obvious. However, a phase shift and increase in wavelength are both more evident.
- A thicker mud layer causes a larger phase lag in the dimensionless vertical wave force on the obstacle surface.

3. Submerged obstacle: Section 3.3

- Due to the vortex generated in the lee of the obstacle of the obstacle, a significantly larger decrease in wave amplitude is shown for transmitted wave component. This is very different from the behaviors observed in the cases of surface or bottom obstacles.
- The largest amplitude attenuation rate occurs at $d_m = \delta_m$ for every wave component.

- With the consideration of a viscous fluid mud bed, the size of the vortex core is considerably smaller and the phase difference on the formation of the vortex can also be observed.
- The case with $d_m = \delta_m$ shows a larger decrease in the dimensionless vertical wave force on the obstacle surface. However, the phase shift is more substantial for a thicker layer with $d_m = 3\delta_m$.

We hope the results presented here provide useful information for the practical design of coastal structures above a muddy seafloor. Of course, there are a number of limitations in our analysis. Above all, three-dimensional problems can be discussed if sufficient computer power is made available to us. In our study, we consider only viscous fluid mud. Nevertheless, our methodology can be extended straightforwardly to account for more complex rheological behaviors of bottom fluid mud since there are many commonly used rheology models available in OpenFOAM, including generalized Newtonian fluid (power law model), viscoelastic fluid (Maxwell model), viscoplastic fluid (Herschel–Bulkley model), among others. To further consider the vertical variation of mud properties, it is also possible to incorporate the multi-layer system of fluid mud bed [81] since the solver we utilize, *multiphaseInterFoam*, can handle flow problems involving multiple incompressible fluids. In order to be more relevant to practical applications, we shall consider obstacles of various shapes and also permeable and flexible structures. This can be achieved by implementing the existing numerical treatments of boundary conditions for porous structures reported in the literature [39]. The present study serves as a preliminary exploration of the impacts of muddy seabeds on wave scattering by engineered structures. Although we elucidate several key underlying physical processes, more numerical investigations and laboratory tests are necessary to eventually provide the technical know-how that can be implemented to develop engineering tools for the design of coastal structures in muddy marine environments.

Author Contributions: Software, validation, formal analysis, and visualization: K.-Y.Z. and C.-W.C. Conceptualization and writing: I.-C.C. All authors have read and agreed to the submitted manuscript.

Funding: This research was funded by the National Science and Technology Council, Taiwan [111-2221-E-002-110].

Conflicts of Interest: The authors declared no conflict of interest.

References

1. Sorensen, R.M. *Basic Coastal Engineering*; Springer: New York, NY, USA, 2006; pp. 209–214.
2. Bea, R.G.; Iversen, R.; Xu, T. Wave-in-deck forces on offshore platforms. *J. Offshore Mech. Arct. Eng.* **2001**, *123*, 10–21. [[CrossRef](#)]
3. Chella, M.A.; Tørum, A.; Myrhaug, D. An overview of wave impact forces on offshore wind turbine substructures. *Energy Procedia* **2012**, *20*, 217–226. [[CrossRef](#)]
4. Kunisu, H. Evaluation of wave force acting on submerged floating tunnels. *Procedia Eng.* **2010**, *4*, 99–105. [[CrossRef](#)]
5. Liu, Y.; Zheng, S.; Liang, H.; Cong, P. Wave interaction and energy absorption from arrays of complex-shaped point absorbers. *Phys. Fluids*. **2022**, *34*, 097107. [[CrossRef](#)]
6. Guo, X.; Wang, B.; Mei, C.C.; Liu, H. Scattering of periodic surface waves by pile-group supported platform. *Ocean Eng.* **2017**, *146*, 46–58. [[CrossRef](#)]
7. Mei, C.C.; Black, J.L. Scattering of surface waves by rectangular obstacles in waters of finite depth. *J. Fluid Mech.* **1969**, *38*, 499–511. [[CrossRef](#)]
8. Siew, P.F.; Hurley, D.G. Long surface waves incident on a submerged horizontal plate. *J. Fluid Mech.* **1977**, *83*, 141–151. [[CrossRef](#)]
9. Ijima, T.; Ozaki, S.; Eguchi, Y.; Kobayashi, A. Breakwater and quay well by horizontal plates. In Proceedings of the 12th Conference on Coastal Engineering, Washington, DC, USA, 13–18 September 1970; pp. 1537–1556.
10. Liu, P.L.-F.; Iskandarani, M. Scattering of short-wave groups by submerged horizontal plate. *J. Waterw. Port Coast. Ocean Eng.* **1991**, *117*, 235–246. [[CrossRef](#)]
11. Cheong, H.-F.; Shankar, N.J.; Nallayarasu, S. Analysis of submerged platform breakwater by eigenfunction expansion method. *Ocean Eng.* **1996**, *23*, 649–666. [[CrossRef](#)]
12. Bautista, E.; Bahena-Jimenez, S.; Quesada-Torres, A.; Méndez, F.; Arcos, E. Interaction between long water waves and two fixed submerged breakwaters of wavy surfaces. *Wave Motion* **2022**, *112*, 102926. [[CrossRef](#)]

13. Williams, K.J. An experimental study of wave-obstacle interaction in a two-dimensional domain. *J. Hydraul. Res.* **1988**, *26*, 463–482. [[CrossRef](#)]
14. Murali, K.; Mani, J.S. Performance of Cage Floating Breakwater. *J. Waterw. Port Coast. Ocean Eng.* **1997**, *123*, 172–179. [[CrossRef](#)]
15. Kagemoto, H.; Fujino, M.; Murai, M. Theoretical and experimental predictions of the hydroelastic response of a very large floating structure in waves. *Appl. Ocean Res.* **1998**, *26*, 135–144. [[CrossRef](#)]
16. Martinelli, L.; Ruol, P.; Zanuttigh, B. Wave basin experiments on floating breakwaters with different layouts. *Appl. Ocean Res.* **2008**, *30*, 199–207. [[CrossRef](#)]
17. Jalos, P. The passage of waves over a bar. *Houille Blanche* **1960**, *15*, 247–267.
18. Dick, T.M.; Brebner, A. Solid and permeable submerged breakwaters. In Proceedings of the 11th Conference on Coastal Engineering, London, UK, 16–20 September 1968; pp. 1141–1158.
19. Rey, V.; Belzons, M.; Guazzelli, E. Propagation of surface gravity waves over a rectangular submerged bar. *J. Fluid Mech.* **1992**, *235*, 453–479. [[CrossRef](#)]
20. Ting, F.C.K.; Kim, Y.-K. Vortex generation in water waves propagating over a submerged obstacle. *Coast. Eng.* **1994**, *24*, 23–49. [[CrossRef](#)]
21. Chang, K.-A.; Hsu, T.-J.; Liu, P.L.-F. Vortex generation and evolution in water waves propagating over a submerged rectangular obstacle: Part I. Solitary waves. *Coast. Eng.* **2001**, *44*, 13–36. [[CrossRef](#)]
22. Chang, K.-A.; Hsu, T.-J.; Liu, P.L.-F. Vortex generation and evolution in water waves propagating over a submerged rectangular obstacle: Part II: Cnoidal waves. *Coast. Eng.* **2005**, *52*, 257–283. [[CrossRef](#)]
23. Rey, V.; Touboul, J. Forces and moment on a horizontal plate due to regular and irregular waves in the presence of current. *Appl. Ocean Res.* **2011**, *33*, 88–99. [[CrossRef](#)]
24. Durgin, W.W.; Shiau, J.C. Wave induced pressures on submerged plates. *J. Waterways Harbors Coast. Eng.* **1975**, *101*, 59–71. [[CrossRef](#)]
25. Patarapanich, M.; Cheong, H.-F. Reflection and transmission characteristics of regular and random waves from a submerged horizontal plate. *Coast. Eng.* **1989**, *13*, 161–182. [[CrossRef](#)]
26. Koraim, A.S. Hydrodynamic efficiency of suspended horizontal rows of half pipes used as a new type breakwater. *Ocean Eng.* **2013**, *64*, 1–22. [[CrossRef](#)]
27. Lo, H.-Y.; Liu, P.L.-F. Solitary waves incident on a submerged horizontal plate. *J. Waterw. Port Coast. Ocean Eng.* **2014**, *140*, 04014009. [[CrossRef](#)]
28. Hayatdavoodi, M.; Ertekin, R.C. Wave forces on a submerged horizontal plate—Part II: Solitary and cnoidal waves. *J. Fluids Struct.* **2015**, *54*, 580–596. [[CrossRef](#)]
29. Durgin, W.W.; Shiau, J.C. Wave induced pressures on a submerged horizontal plate. In Proceedings of the 5th Annual Offshore Technology Conference, Houston, TX, USA, 28 April 28–1 May 1973; pp. 1141–1158.
30. Touboul, J.; Rey, V. Bottom pressure distribution due to wave scattering near a submerged obstacle. *J. Fluids Mech.* **2012**, *702*, 444–459. [[CrossRef](#)]
31. Gao, H.; Song, Y.; Fang, Q.; Li, S. Wave forces on box-girder-type bridge deck located behind trench or breakwater. *Ocean Eng.* **2021**, *237*, 109618. [[CrossRef](#)]
32. Liu, P.L.-F.; Abbaspour, M. An integral equation method for the diffraction of oblique waves by an infinite cylinder. *Int. J. Numer. Methods Eng.* **1982**, *18*, 1497–1504. [[CrossRef](#)]
33. Patarapanich, M. Forces and moment on a horizontal plate due to wave scattering. *Coast. Eng.* **1984**, *8*, 279–301. [[CrossRef](#)]
34. Grue, J. Nonlinear water waves at a submerged obstacle or bottom topography. *J. Fluid Mech.* **1992**, *244*, 455–476. [[CrossRef](#)]
35. Wang, K.-H.; Wu, T.Y.; Yates, G.T. Three-dimensional scattering of solitary waves by vertical cylinder. *J. Waterw. Port Coast. Ocean Eng.* **1992**, *118*, 551–566. [[CrossRef](#)]
36. Lynett, P.; Liu, P.L.-F. A two-layer approach to water wave modeling. *Proc. R. Soc. Lond. A Math. Phys. Sci.* **2004**, *460*, 2637–2669. [[CrossRef](#)]
37. Huang, C.-J.; Dong, C.-M. On the interaction of a solitary wave and a submerged dike. *Coast. Eng.* **2001**, *43*, 265–286. [[CrossRef](#)]
38. Lin, P. A numerical study of solitary wave interaction with rectangular obstacles. *Coast. Eng.* **2004**, *51*, 35–51. [[CrossRef](#)]
39. Higuera, P.; Lara, J.L.; Losada, I.J. Three-dimensional interaction of waves and porous coastal structures using OpenFOAM®. Part I: Formulation and validation. *Coast. Eng.* **2014**, *83*, 243–258. [[CrossRef](#)]
40. Higuera, P.; Lara, J.L.; Losada, I.J. Three-dimensional interaction of waves and porous coastal structures using OpenFOAM®. Part II: Application. *Coast. Eng.* **2014**, *83*, 259–270. [[CrossRef](#)]
41. Dean, R.G.; Dalrymple, R.A. *Water Wave Mechanics for Engineers and Scientists*; World Scientific: Singapore, 1991; pp. 261–262.
42. Wang, Y.; Healy, T.; Members of SCOR Working Group 106. In *Muddy Coasts of the World: Processes, Deposits and Function*; Healy, T., Wang, Y., Healy, J.-A., Eds.; Elsevier: Amsterdam, The Netherlands, 2002; Chapter 2, pp. 9–18.
43. Jeng, D.-S. *Porous Models for Wave-Seabed Interactions*; Springer: Berlin/Heidelberg, Germany, 2013; pp. 1–4.
44. Mohapatra, S. Effects of elastic bed on hydrodynamic forces for a submerged sphere in an ocean of finite depth. *Z. Angew. Math. Phys.* **2017**, *68*, 91. [[CrossRef](#)]
45. Das, L.; Mohapatra, S. Effects of flexible bottom on radiation of water waves by a sphere submerged beneath an ice-cover. *Meccanica* **2019**, *54*, 985–999. [[CrossRef](#)]

46. Barman, K.K.; Bora, S.N. Interaction of oblique water waves with a single chamber caisson type breakwater for a two-layer fluid flow over an elastic bottom. *Ocean Eng.* **2021**, *238*, 109766. [[CrossRef](#)]
47. Sarkar, B.; Paul, S.; De, S. Effects of flexible bed on oblique wave interaction with multiple surface-piercing porous barriers. *Z. Angew. Math. Phys.* **2021**, *72*, 83. [[CrossRef](#)]
48. Bierawski, L.G.; Maeno, S. VOF-FEM numerical model of submerged breakwater on permeable bottom. *J. Appl. Mech.* **2004**, *7*, 945–952. [[CrossRef](#)]
49. Maiti, P.; Mandal, B.N. Water wave scattering by an elastic plate floating in an ocean with a porous bed. *Appl. Ocean Res.* **2014**, *47*, 73–84. [[CrossRef](#)]
50. Koley, S.; Sahoo, T. Wave interaction with a submerged semicircular porous breakwater placed on a porous seabed. *Eng. Anal. Bound. Elem.* **2017**, *80*, 18–37. [[CrossRef](#)]
51. Behera, H.; Ng, C.-O.; Sahoo, T. Oblique wave scattering by a floating elastic plate over a porous bed in single and two-layer fluid systems. *Ocean Eng.* **2018**, *159*, 280–294. [[CrossRef](#)]
52. Barman, K.K.; Bora, S.N. Scattering and trapping of water waves by a composite breakwater placed on an elevated bottom in a two-layer fluid flowing over a porous sea-bed. *Appl. Ocean Res.* **2021**, *113*, 102544. [[CrossRef](#)]
53. Chanda, A.; Bora, S.N. Scattering of flexural gravity waves by a pair of submerged vertical porous barriers located above a porous sea-bed. *J. Offshore Mech. Arct. Eng.* **2022**, *144*, 011201. [[CrossRef](#)]
54. Mynett, A.E.; Mei, C.C. Wave-induced stresses in a saturated poro-elastic sea bed beneath a rectangular caisson. *Géotechnique* **1982**, *32*, 235–247. [[CrossRef](#)]
55. Tsai, Y.T.; McDougal, W.G.; Sollitt, C.K. Response of finite depth seabed to waves and caisson motion. *J. Waterw. Port Coast. Ocean Eng.* **1990**, *116*, 1–20. [[CrossRef](#)]
56. Mase, H.; Sakai, T.; Sakamoto, M. Wave-induced porewater pressures and effective stresses around breakwater. *Ocean Eng.* **1994**, *21*, 361–379. [[CrossRef](#)]
57. Mizutani, N.; Mostafa, A.M.; Iwata, K. Nonlinear regular wave, submerged breakwater and seabed dynamic interaction. *Coast. Eng.* **1999**, *33*, 177–202. [[CrossRef](#)]
58. Mostafa, A.M.; Mizutani, N.; Iwata, K. Nonlinear wave, composite breakwater, and seabed dynamic interaction. *J. Waterw. Port Coast. Ocean Eng.* **1999**, *125*, 88–97. [[CrossRef](#)]
59. Kumagai, T.; Foda, M.A. Analytical model for response of seabed beneath composite breakwater to wave. *J. Waterw. Port Coast. Ocean Eng.* **2002**, *128*, 62–71. [[CrossRef](#)]
60. Jeng, D.-S.; Schacht, C.; Lemckert, C. Experimental study on ocean waves propagating over a submerged breakwater in front of a vertical seawall. *Ocean Eng.* **2005**, *32*, 2231–2240. [[CrossRef](#)]
61. Tsai, C.-P.; Chen, H.-B.; Lee, F.-C. Wave transformation over submerged permeable breakwater on porous bottom. *Ocean Eng.* **2006**, *33*, 1623–1643. [[CrossRef](#)]
62. Tsai, C.-P.; Chen, H.-B.; Jeng, D.-S. Wave attenuation over a rigid porous medium on a sandy seabed. *J. Eng. Mech.* **2009**, *135*, 1295–1304. [[CrossRef](#)]
63. Jeng, D.-S.; Ye, J.-H.; Zhang, J.-S.; Liu, P.L.-F. An integrated model for the wave-induced seabed response around marine structures: Model verifications and applications. *Coast. Eng.* **2013**, *72*, 1–19. [[CrossRef](#)]
64. Li, Y.; Ong, M.C.; Tang, T. A numerical toolbox for wave-induced seabed response analysis around marine structures in the OpenFOAM® framework. *Ocean. Eng.* **2010**, *195*, 106678. [[CrossRef](#)]
65. Jeng, D.-S.; Wang, X.; Tsai, C.-C. Meshless model for wave-induced oscillatory seabed response around a submerged breakwater due to regular and irregular wave loading. *J. Mar. Sci. Eng.* **2021**, *9*, 9010015. [[CrossRef](#)]
66. Gade, H.G. Effects of a non-rigid, impermeable bottom on plane surface waves in shallow water. *J. Mar. Res.* **1958**, *16*, 61–82.
67. Soltanpour, M.; Haghshenas, S.A. Fluidization and representative wave transformation on muddy beds. *Cont. Shelf Res.* **2009**, *29*, 666–675. [[CrossRef](#)]
68. Dalrymple, R.A.; Liu, P.L.-F. Waves over soft muds: A two layer model. *J. Phys. Oceanogr.* **1978**, *8*, 1121–1131. [[CrossRef](#)]
69. MacPherson, H. The attenuation of water waves over a non-rigid bed. *J. Fluid Mech.* **1980**, *97*, 721–742. [[CrossRef](#)]
70. Ng, C.-O. Water waves over a muddy bed: A two-layer Stokes' boundary layer model. *Coast. Eng.* **2000**, *40*, 221–242. [[CrossRef](#)]
71. Mei, C.C.; Liu, K.-F. A Bingham-plastic model for a muddy seabed under long waves. *J. Geophys. Res.* **1987**, *92*, 14581–14594. [[CrossRef](#)]
72. Liu, K.-F.; Mei, C.C. Effects of wave-Induced friction on a muddy seabed modelled as a Bingham-plastic fluid. *J. Coast. Res.* **1989**, *5*, 777–789.
73. Higuera, P. olaflow: CFD for Waves [Computer Software]. 2017. Available online: <https://zenodo.org/record/1297013#Y1JNUUxBxPY> (accessed on 8 August 2022).
74. Weller, H.G.; Tabor, G.; Jasak, H.; Fureby, C. A tensorial approach to computational continuum mechanics using object-oriented techniques. *Comput. Phys.* **1998**, *12*, 620–631. [[CrossRef](#)]
75. Higuera, P. Enhancing active wave absorption in RANS models. *Appl. Ocean Res.* **2000**, *94*, 102000. [[CrossRef](#)]
76. Soltanpour, M.; Shamsnia, S.H.; Shibayama, T.; Nakamura, R. A study on mud particle velocities and mass transport in wave-current-mud interaction. *Appl. Ocean Res.* **2018**, *78*, 267–280. [[CrossRef](#)]
77. Goda, Y.; Suzuki, Y. Estimation of incident and reflected waves in random wave experiments. In Proceedings of the 15th Coastal Engineering Conference, Honolulu, HI, USA, 11–17 July 1976; pp. 828–845.

78. Mansard, E.P.D.; Funke, E.R. The measurement of incident and reflected spectra using a least squares method. In Proceedings of the 17th Coastal Engineering Conference, Sydney, Australia, 23–28 March 1980; pp. 154–172.
79. Zelt, J.A.; Skjelbreia, J. Estimating incident and reflected wave fields using an arbitrary number of wave gauges. In Proceedings of the 23rd Coastal Engineering Conference, Venice, Italy, 4–9 October 1992; pp. 777–789.
80. Brossard, J.; Hemon, A.; Rivoalen, E. Improved analysis of regular gravity waves and coefficient of reflexion using one or two moving probes. *Coast. Eng.* **2000**, *39*, 193–212. [[CrossRef](#)]
81. Maa, J.P.-Y.; Mehta, A.J. Mud erosion by waves: A laboratory study. *Cont. Shelf Res.* **1987**, *7*, 1269–1284. [[CrossRef](#)]